



Power Electronic Systems
Laboratory

© 2016 IEEE

IEEE Journal of Emerging and Selected Topics on Power Electronics (JESTPE), Vol. 4, No. 4, pp. 1370-1382, December 2016

Multi-Objective Optimization of 50 kW/85 kHz IPT System for Public Transport

R. Bosshard,
J. W. Kolar

This material is published in order to provide access to research results of the Power Electronic Systems Laboratory / D-ITET / ETH Zurich. Internal or personal use of this material is permitted. However, permission to reprint/republish this material for advertising or promotional purposes or for creating new collective works for resale or redistribution must be obtained from the copyright holder. By choosing to view this document, you agree to all provisions of the copyright laws protecting it.



Eidgenössische Technische Hochschule Zürich
Swiss Federal Institute of Technology Zurich

Multi-Objective Optimization of 50 kW/85 kHz IPT System for Public Transport

Roman Bosshard, *Student Member, IEEE*, and Johann W. Kolar, *Fellow, IEEE*

Abstract—Inductive power transfer (IPT) is an attractive solution for the automated battery charging of public transport electric vehicles (EVs) with low maintenance requirements. This paper presents the design of a 50 kW/85 kHz contactless EV charger, with a focus on the IPT transmitter and receiver coils. The multi-objective magnetics optimization reveals the Pareto tradeoffs and performance limitations in terms of high efficiency, high power density, and low stray field for high-power IPT systems without moving mechanical parts. A full-scale hardware prototype is realized and experimentally investigated. The dc–dc conversion efficiency, including all the power electronics stages, is measured as 95.8% at 50 kW power transfer across an air gap of 160 mm (coil dimensions 410 × 760 × 60 mm³). With 150 mm coil misalignment in the worst case direction, the dc–dc efficiency drops to 92%. The measurements of the magnetic stray field show compliance with ICNIRP 2010 at 800 mm distance from the IPT coil center.

Index Terms—Electric vehicles, inductive power transmission, pareto optimization.

I. INTRODUCTION

ELECTRIC mobility is rapidly gaining popularity owing to the increasing CO₂-awareness and the lower total cost of ownership of electric vehicles (EVs). Rising market shares of EV among newly sold vehicles document the trend toward more sustainable ways of transportation [1], [2]. In urban public transport, a shift from conventional fossil fuel-powered vehicles and trolleybuses toward plug-in hybrid and battery electric buses is underway [3], [4]. Reduced exhaust emissions, more quiet operation, and less visible infrastructure, e.g., no overhead lines for the power supply of trolleybuses, are the key advantages of electric transportation in urban environments. In addition, lower operating cost and lower fuel price volatility result from using electrical energy instead of diesel fuel or petroleum as a primary energy source. As the main disadvantage, the required on-board electric energy storage presents a major share of the initial cost. Furthermore, in comparison with conventional fossil-fuelled vehicles, plug-in EV confronts operators with extended dwell times for the recharging of the large battery at the bus depot.

Manuscript received March 24, 2016; revised June 30, 2016; accepted August 1, 2016. Date of publication August 10, 2016; date of current version October 28, 2016. This work was supported by ABB Switzerland Ltd. Recommended for publication by Associate Editor Chun T. Rim.

R. Bosshard was with the Power Electronic Systems Laboratory, Swiss Federal Institute of Technology Zurich, 8092 Zürich, Switzerland. He is now with ABB Switzerland Ltd., ABB Switzerland Ltd., 5300 Turgi, Switzerland, Switzerland (e-mail: roman.bosshard@gmail.com).

J. W. Kolar is with the Power Electronic Systems Laboratory, Swiss Federal Institute of Technology Zurich, 8092 Zürich, Switzerland (e-mail: kolar@lem.ee.ethz.ch).

Color versions of one or more of the figures in this paper are available online at <http://ieeexplore.ieee.org>.

Digital Object Identifier 10.1109/JESTPE.2016.2598755

With the goal of reducing the necessary battery volume and the dwell time, several vehicle equipment manufacturers have recently presented *opportunity charging* concepts that shift the charging process from the bus depot to automated charging stations that are distributed at bus stations, taxicab stands, or traffic lights along the bus route [5]–[10]. Due to the integration of the charging with the regular operation of the EV, a significant reduction of the necessary charging time at the bus depot is possible. In addition, the more frequent charging intervals can be utilized to reduce the on-board energy storage capacity, while they also have a beneficial effect on the lifetime of the battery as a result of the lower depth of discharge [11].

For a practical realization, a quick, reliable, and automated way for initiating the charging process is needed. The solutions presented in [5] and [6] rely on moving mechanical components to establish a galvanic connection between the isolated dc output of the charging station and the charging controller located on the vehicle. However, these systems suffer from mechanical wear and fatigue, as well as from the corrosion of the exposed metal contacts that interface the charging station with the on-board power electronics. As an alternative without a galvanic connection, contactless battery charging systems using inductive power transfer (IPT) have been proposed for public transport [7]–[10], [12], [13]. In IPT systems, the charging cable is replaced by inductively coupled transmission coils. A high-frequency ac current in a transmitter coil embedded in the road surface is used to transfer charging energy across the air gap given by the vehicle ground clearance to a receiver coil mounted to the EV chassis by magnetic induction.

Due to the high power levels of 100–200 kW, in [7] and [8], the receiver coil is mechanically lowered to the road surface in order to reduce the air gap between the coils. This increases the transmission efficiency and it reduces the high-frequency electromagnetic stray fields in the environment surrounding the charging platform, but the disadvantages of moving mechanical parts remain. With an ample number of opportunity charging stations along the bus route, also a lower charging power can be sufficient. For power levels around 50 kW, IPT systems can be practically realized without moving mechanical parts [9]. This lowers the maintenance requirements for the mechanical components and thereby reduces operating cost.

Independent of the employed technology, the EV charging equipment must satisfy automotive requirements, such as low cost, high reliability, and high compactness. For minimum energy cost, a high charging efficiency is mandatory. For contactless EV chargers, the main challenges in fulfilling these

requirements result from the tradeoff between the compactness of the employed transmission coils and the efficiency of the power transfer [14], [15]. In order to achieve a high magnetic coupling and a high transmission efficiency, the physical dimensions of IPT coils have to be large compared with the ground clearance of the vehicle. However, in practice, this is often not possible.

On the one hand, the available construction volume is typically limited because of the necessary integration of the IPT receiver coil into the EV chassis. Then, a more compact coil design with a higher power density and consequently higher losses must be used. On the other hand, also the high-frequency magnetic stray field is linked to the coil size and the efficiency by a tradeoff [14]. Smaller IPT coils present a smaller magnetic field source and, therefore, simplify shielding. As opportunity charging stations need to be installed at locations that are accessible by the public, e.g., at bus stations, high safety requirements apply. Hence, at a sufficiently high power level, more compact IPT coils may become mandatory in order to fulfill the relevant stray field norms [16].

Compact IPT coils present a particular challenge as their thermal management is a difficult task. For instance, metal heat sinks placed in close proximity to the magnetic parts can be subject to induced eddy currents that cause additional heating and further decrease the efficiency. In order to simplify the thermal management, an optimized magnetics design is crucial for ensuring minimum power losses in the IPT coils. However, also the selection of the power electronics topology as well as the employed modulation and control schemes has an impact on the winding currents and on the power losses in the coils. Therefore, only a comprehensive system optimization taking all of these aspects into account can provide a meaningful picture of the attainable performance of an IPT system.

A number of recent publications discuss IPT systems with charging power levels suitable for public transport EV [17]–[20]. However, a holistic system optimization or an analysis of the performance limits of IPT systems in face of the listed restrictions has not been presented so far. Typically, only selected aspects are considered instead of a comprehensive analysis of all relevant performance factors and available degrees of freedom. Therefore, it is also not clear how a fully optimized IPT system compares with a conventional conductive charging solution in terms of the attainable component size, transmission efficiency, material effort, and cost. The target of the industry research project that underlies this publication is therefore to answer these questions and to determine the best possible performance for an exemplary 50 kW public transport IPT system. Hence, this paper presents the design of a technology demonstrator that is fully optimized and provides a benchmark for such a performance comparison. This paper is mainly focused on the magnetics design, while the design of the power electronics is only briefly summarized. A detailed discussion of the power converter and the employed control can be found in a separate paper [21]. The complete documentation of the work is contained in [22].

TABLE I
SPECIFICATIONS OF THE DESIGNED IPT SYSTEM

Parameter	Variable	Value
Output Power	P_2	50 kW
Transmitter-Side DC-Voltage	$U_{1,dc}$	0-800 V
Receiver-Side DC-Voltage	$U_{2,dc}$	0-800 V
Battery Voltage	U_{batt}	500-700 V
Air Gap	z	100-200 mm
Positioning Tolerance	$\Delta x, y$	± 150 mm
Transmission Frequency	f_0	85 kHz

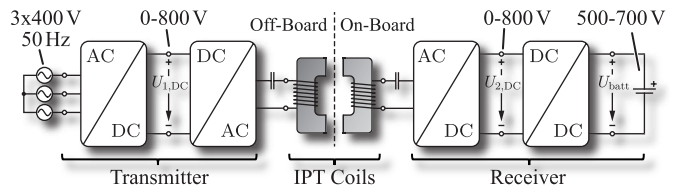


Fig. 1. IPT system power conversion chain from the European 400 V/50 Hz three-phase mains to the high-voltage battery of the public transport EV (reproduced from [21]).

A multi-objective design process for IPT systems was first presented and practically verified with the design of a laboratory scale prototype in [14]. In this paper, the approach is applied to the design of a full-scale 50 kW contactless charger for a public transport application with the specifications listed in Table I and the power electronics architecture in Fig. 1. The main requirement for the optimization is comprehensive component and system models for calculating the considered performance factors. Therefore, in Section II, analytical models are derived for the calculation of the winding losses of a novel rectangular coil geometry. For including the power losses in the core and shielding materials, and in order to estimate the magnetic stray field, the analytical models are combined with the 3-D finite element method (FEM) simulations. Additional models are developed for the estimation of the winding and core temperatures.

In Section III, a detailed description of the multi-objective optimization of the IPT coils is presented. The encountered tradeoffs, parameter interdependences, and performance limits are highlighted and analyzed in a detailed discussion. A forced-air cooled IPT coil design with the dimension of $410 \times 760 \times 60$ mm³, a total weight of 24.6 kg, an area-related power density of 1.6 kW/dm², and a gravimetric power density of 2 kW/kg (or 907 W/lb) is selected from the optimization results and a hardware prototype is realized. In Section IV, the details on the prototype realization are presented and an overview of the measurement setup employed for the testing up to the rated power of 50 kW is given. Afterward, in Section V, the experimental results obtained from the prototype system are presented. A maximum dc–dc efficiency of 95.8% is measured for the transmission of 50 kW across an air gap of 160 mm with ideally aligned IPT coils, including the coil losses, the losses of the resonant capacitors, the eddy current shielding, and the losses of the

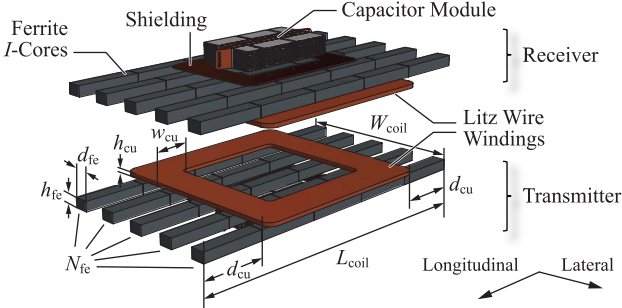


Fig. 2. Proposed rectangular IPT coil geometry including the resonant capacitor module (transmitter and receiver are identical). Degrees of freedom available for the multi-objective optimization are indicated.

power electronics. The dc–dc efficiency drops to 92% for a coil misalignment of 150 mm in the worst case direction. The measurements of the magnetic stray field confirm compliance with the considered standard [16].

Finally, in Section VI, the main conclusions obtained from this paper are summarized. A general discussion of the results and an outlook on the future of contactless EV charging is additionally found in [23].

II. COIL GEOMETRY AND POWER LOSS MODELING

A precondition for the multi-objective optimization process described in [14] is the comprehensive models for calculating the power losses in the IPT coil, the component temperatures, and the magnetic stray field of the coil arrangement. In this section, an analytical model for the high-frequency winding losses is derived for the considered IPT coil geometry. The winding loss calculation is combined with the 3-D FEM simulations for incorporating the losses in the cores and the eddy current shielding, as well as for estimating the magnetic stray field.

A. Selection of the Coil Geometry

The rectangular coil geometry of Fig. 2 is proposed. Due to its rectangular shape, this coil geometry allows optimally utilizing a rectangular construction volume on the EV. With a circular coil geometry, the corners of a rectangular construction volume are not used for the contactless power transfer. Therefore, depending on the aspect ratio of the construction volume in the considered industry application, a rectangular coil geometry may lead to an improved magnetic coupling. In addition, the proposed coil geometry consists only of a planar core structure and a single planar litz wire winding, which simplifies the manufacturing process. The focus of this paper is on the multi-objective optimization process. Therefore, a detailed performance comparison of the proposed IPT coil geometry and the frequently discussed *double-D* coil layout of [24]–[27] is the subject of a separate publication [28].

Only single layer coils are considered because of their low profile and the low self-capacitance. As proposed in [29], the ferrite core is split into several separated bars, which are practically realized by aligning multiple *I*-cores. This reduces the core weight significantly when compared with a single core that completely covers the backside of the winding.

The splitting of the core only has a small effect on the field distribution and the magnetic properties as a result of the high relative permeability of the core material.

The resonant capacitors are assembled in a compact, forced-air cooled module that is mounted to the backside of the IPT coils. The magnetic field at the location of the resonant capacitor is relatively high despite the ferrite cores. Therefore, a shielding plate made from oxygen-free copper (conductivity approximately 43 MS/m) is placed as an eddy current shielding between the ferrite bars and the capacitors. The details on the dimensioning of the shielding are given in [22].

In order to facilitate the experimental verification at 50 kW, a measurement setup with energy feedback through a dc connection between the transmitter-side and receiver-side dc-link terminals is considered in this paper (see Section IV). In order to limit the necessary hardware effort, a symmetrical system with identical power electronics and IPT coils for the transmitter and the receiver is preferred. The presented coil prototype is intended as the receiver coil. In a final realization, a different layout could be considered for the transmitter coil, e.g., comprising multiple selectively activated windings for increasing the positioning tolerance. The methods and the results presented in this paper can also be applied to such a configuration.

B. Employed 3-D FEM Models

Since the proposed coil geometry has no 2-D symmetry, the prototype coils have to be analyzed with the 3-D FEM models. This requires model simplifications for the power loss estimation, because the 3-D FEM simulations are significantly more computationally intensive than the 2-D calculations. A simplification that is common for simulating conventional transformers or electrical machines is to model the copper windings as a solid copper region with the same current density than in the original conductors.

A similar approximation can also be used for the 3-D FEM models of IPT coils (see Fig. 2). Because the windings are not modeled in full detail, the required calculation time is lower than for the initially much more complex 3-D model. The magnetic field outside the winding is still calculated accurately if the geometries of the solid copper regions approximately match the outer dimensions of the actual windings and the total winding current remains constant. In this case, the current density in the simplified model is not the same as in the actual winding. Therefore, an evaluation of the FEM results for the estimation of the ac resistance and the power losses in the litz wire winding is no longer accurately possible due to the model simplifications. As an alternative method for calculating the losses in the windings, an analytical winding loss model is derived in Section II-C.

The calculation of the magnetic energy remains sufficiently accurate despite the simplifications. Therefore, the self-inductances L_1 and L_2 , the mutual inductances M , and the magnetic coupling k can be predicted with the simplified model. The validity of the approximation is confirmed by the comparison of the FEM-calculated transformer equivalent circuit parameters obtained from the tool Ansys Maxwell and

TABLE II
MEASURED AND CALCULATED EQUIVALENT CIRCUIT PARAMETERS

Variable	Measured	Calculated	Error
L_1	$68.2 \mu\text{H}$	$71.6 \mu\text{H}$	+1.4%
L_2	$70.6 \mu\text{H}$	$71.6 \mu\text{H}$	+5.0%
M	$15.4 \mu\text{H}$	$16.5 \mu\text{H}$	+7.4%
k	0.2214	0.2318	+4.7%

the parameters measured for the realized hardware prototype, as given in Table II.

Since the magnetic field outside the winding is still accurate, the power losses in the employed ferrite cores can be calculated by the integration of the Steinmetz core loss density, and also the losses in the eddy current shielding can be obtained from the FEM tool.

C. Analytical Winding Loss Model

For the calculation of the power losses due to the skin and proximity effects, the models in [30] are used. For taking into account the external proximity effect, the external magnetic field in the litz wire conductors must be calculated. The magnetic fields in the transmitter and receiver coil windings are calculated separately. This is possible, because the fields are mainly caused by the current in the neighboring conductors within the same winding and only a negligible part results from the current in the opposite IPT coil, which is a result of the large air gap.

As shown in Fig. 3(a), three 2-D cut surfaces (labeled A, B, and C) are defined in the 3-D model of a single IPT coil. The magnetic field on the three cut surfaces is calculated approximatively. The geometry of the cut surface is assumed as infinitely extended in the direction of the plane, and the corner effects are neglected. Furthermore, the dc current distribution in the conductors and the dc magnetic field is used. This is valid if the litz wire strand diameter is chosen small compared with the skin depth at the considered operating frequency. Infinite permeability is assumed for the ferrite cores, which is a good approximation given the actual relative permeability of $\mu_{r,\text{fe}} \approx 2000$. The cores are assumed to be nonconductive, and the field distortions due to eddy currents in the cores are neglected.

Using these approximations, the magnetic field on the cut surfaces A, B, and C is calculated by solving Ampère's law for each conductor separately. For cut surface A, the y -component of the magnetic field along the x -axis through the conductor centers (see Fig. 3(c)), caused by conductor $i = 1, 2, \dots, N$ located at position $x = x_i$ and carrying the current \hat{I}_i , results as

$$\hat{H}_y(x, x_i) = \begin{cases} \hat{I}_i(x - x_i) / \left(\frac{1}{2} \pi d_a^2 \right), & \text{for } |x - x_i| < d_a/2 \\ \hat{I}_i/(2\pi(x - x_i)), & \text{otherwise} \end{cases} \quad (1)$$

where d_a represents the outer diameter of the conductor. The complete magnetic field is given by the superposition of the results for all N conductors. For cut surface A, in which no core elements are contained, this calculation is straightforward

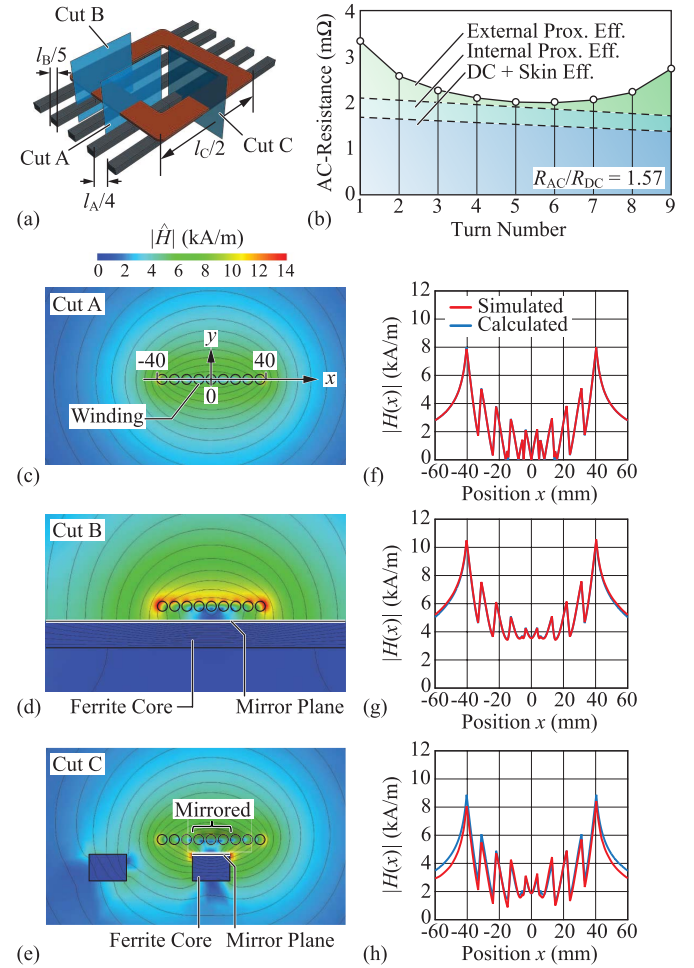


Fig. 3. (a) Definition of the cut surfaces A, B, and C used for the estimation of the ac losses. (b) Calculated ac resistance for each turn of the winding of the realized prototype IPT coil. (c)–(e) FEM-calculated magnetic field distribution. (f)–(h) Comparison with the analytically calculated magnetic field for a current of 100 A.

and the analytically calculated solution matches the result of the 2-D FEM calculation in Fig. 3(f) exactly.

The surfaces B and C cut through core elements, which alter the field distribution in the winding. To capture the effects of the cores, the *mirroring* (or *imaging*) method is applied [30], [31]. On cut surface B, the winding is mirrored at the core surface, as shown in Fig. 3(d). The magnetic field of the mirrored conductors is calculated using (1) (modified to 2-D vector notation) and added to the solution for cut surface A. This approximation is valid as long as the permeability of the core is significantly higher than that of the surrounding medium. The calculated result is compared with the result of the FEM simulation in Fig. 3(g). Also for the calculation on cut surface B, good agreement with the FEM results is achieved.

For cut surface C, the imaging method is applied only for the core that is positioned below the winding. The effect of the second core, which is located outside the winding, is neglected in order to simplify the analysis. For the example shown in Fig. 3(e), the three central conductors of the winding that are positioned vertically above the core are mirrored at the

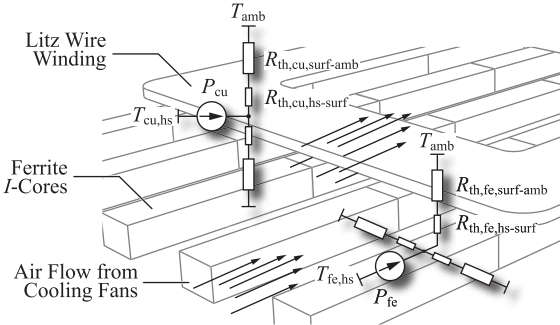


Fig. 4. Simplified thermal model for the estimation of the hotspot temperatures in the litz wire winding and the ferrite cores of the IPT coils.

core surface. Like for cut surface B, the field of the mirrored conductors is added to the solution for cut surface A. Also in this case, the agreement between the calculated result and the FEM analysis shown in Fig. 3(h) is satisfactory.

The ac power losses are calculated for each turn of the winding and for each of the cut surfaces A, B, and C individually. For the estimation of the power losses due to the external proximity effect, the magnetic field obtained from the analytical calculation described earlier is evaluated at the center of each conductor. For the internal proximity effect in the litz wires and for the skin effect, the analytical models in [30] are used. The ac resistances per unit length that are calculated on each cut surface are multiplied by the length contribution l_A , l_B , and l_C of the respective cut surface to the total length of each conductor and added up to obtain the ac resistance of every conductor in the winding (see Fig. 3(a)).

The result of the calculation is shown in Fig. 3(b) for each of the nine turns in the winding of the coil prototype optimized in this paper. The partitioning into dc loss and skin effect, internal proximity effect, and external proximity effect is also given. The turn denoted by turn number 9 is the innermost turn of the winding and has therefore the shortest total conductor length and the lowest dc resistance. The total ac resistance of the winding is obtained as $R_{ac} \approx 22.5 \text{ m}\Omega$ by adding up the ac resistance of each turn. The estimated ac-to-dc resistance ratio is $R_{ac}/R_{dc} \approx 1.57$ at 85 kHz for the winding of the coil prototype with a litz wire comprising $2500 \text{ mm} \times 0.1 \text{ mm}$ strands and outer diameter $d_a = 7.4 \text{ mm}$.

D. Simplified Thermal Model

For the multi-objective optimization, forced convection cooling by axial cooling fans placed at both sides of the coil is assumed (see Fig. 8). The considered thermal model for estimating the winding and core hotspot temperatures $T_{cu,hs}$ and $T_{fe,hs}$ is shown in Fig. 4. The thermal resistance $R_{th,cu,hs-surf}$ models the heat conduction from the hotspot inside the winding to the winding surface. The heat transfer on the winding surface due to the forced convection is represented by the thermal resistance $R_{th,cu,surf-amb}$. Equal models are assumed for the top and bottom winding surfaces. For the ferrite cores, an analogous model is used. In this case, the top surface and the surfaces at the sides of the ferrite cores are considered. For the winding as well as for the cores,

the respective power losses P_{cu} and P_{fe} are assumed to be uniformly distributed over the whole component volume.

The heat transfer via forced convection cooling at the core and winding surfaces is estimated using the models of [32]. The models allow approximating the fluid flow in the air channels between the ferrite cores and the winding and between the topside cover of the coil housing and the winding in the arrangement using the characteristics of cooling fans and the geometric dimension considered in the optimization of Section III. From the result, the heat transfer coefficient at selected channel surfaces can be approximated. The average surface heat transfer coefficient for the winding and the ferrite cores is estimated as $\bar{h}_{cu} \approx 100 \text{ W}/(\text{m}^2\text{K})$ and $\bar{h}_{fe} \approx 100-200 \text{ W}/(\text{m}^2\text{K})$. Therefore, as a conservative model, $\bar{h}_{cu} = \bar{h}_{fe} = 100 \text{ W}/(\text{m}^2\text{K})$ is used. Given these estimates, the maximum surface-related power loss density for the windings and the core is approximately $0.35-0.75 \text{ W/cm}^2$ for an ambient temperature of $T_{amb} = 45^\circ\text{C}$ and surface temperatures between 80°C and 120°C . This is in good agreement with the typical values given in [33].

Due to the complexity of the considered coil arrangement, a more detailed consideration would require coupled magnetics and fluid dynamics FEM simulations. This is omitted in order to accelerate the computations used in the optimization process. The results that are obtained from this simplified calculation are sufficient to assess the thermal feasibility of the IPT coil designs and to provide a fundamental understanding of the main design tradeoffs.

III. MULTI-OBJECTIVE COIL OPTIMIZATION

Based on the presented models, a multi-objective optimization of the coil parameters is conducted in this section. First, the side conditions and the main steps of the optimization process are outlined. Then, the obtained results are presented, which expose the performance limits for the considered system. The characteristic Pareto tradeoffs between the performance factors transmission efficiency, area-related and gravimetric power density, and magnetic stray field encountered at the performance limit are discussed in detail. At the end of this section, a design is selected for the realization of a hardware prototype.

A. Transmission Frequency and Geometric Side Conditions

As shown in [15] and [34], the maximum transmission efficiency of an IPT system is mainly determined by the figure of merit $FOM = kQ$, where k represents the magnetic coupling of the IPT coils and $Q \approx \omega_0 L / R_{ac}$ stands for the coil quality factor at the transmission frequency ω_0 . Therefore, the geometric arrangement and the transmission frequency have a major impact on the attainable system performance.

For interoperability among the products of different manufacturers of IPT equipment, a common transmission frequency of 85 kHz is proposed in the upcoming standard J2954 by the Society of Automotive Engineers (SAE) [35], [36]. A higher transmission frequency can lead to lower coil losses, because the optimum receiver reactance $\omega_0 L_2$ that maximizes the transmission efficiency for a given coil arrangement is obtained at a lower receiver coil inductance L_2 . Hence, fewer

turns are sufficient on the receiver and a lower ac resistance results due to the shorter total conductor length [14]. Furthermore, the flux linkage and, therefore, also the magnetic stray field can be reduced at a higher frequency, because the induced voltage on the receiver is proportional to the product of the frequency and the magnetic flux [14]. However, for demonstrating the attainable performance at the common frequency of the upcoming SAE standard, 85 kHz is selected as the transmission frequency for the prototype designed in this paper.

Considering the ground clearance of typical vehicles, an air gap of approximately 100–200 mm is required for the contactless EV charger. In addition, a positioning tolerance of around ± 150 mm is needed taking into account the parking accuracy of professional public transport drivers. For the optimization, the coils are ideally aligned with an air gap of 160 mm. As a result of the large air gap, a low magnetic coupling must be expected and a resonant compensation of both IPT coils is needed. As shown in Fig. 1, a series-series resonant compensation is used in this paper for the low circulating reactive power during light load conditions and because the fully symmetric topology simplifies the testing with energy feedback described in Section IV. During the optimization, the capacitance values C_1 and C_2 are selected for a full compensation of the coil self-inductances at the transmission frequency by

$$C_1 = 1/(\omega_0^2 L_1) \text{ and } C_2 = 1/(\omega_0^2 L_2). \quad (2)$$

This choice ensures that the converter operates at zero phase angle conditions for any positioning of the IPT coils. For the hardware prototype, the capacitance values are selected slightly larger in order to ensure inductive operation and zero voltage switching (ZVS) of the employed SiC MOSFET devices at the operating frequency. The selected capacitance values are given in Table III.

B. Multi-Objective Optimization Process

In the following, the multi-objective optimization process outlined in Fig. 5 is used to find suitable values for the degrees of freedom of the coil geometry shown in Fig. 2.

First, the electric and constructive boundary conditions are specified, and the material data are defined (steps 1–3). For the permeability and the Steinmetz parameters of the cores, the ferrite material K2004 is considered. In order to lower the number of parameters, the dimensions $h_{fe} = 20$ mm and $d_{fe} = 28$ mm of the cores are kept constant at the values of the core I-126/20 [37]. The litz wire strand diameter is preselected as 0.1 mm, taking into account the skin depth of $\delta \approx 0.23$ mm at the transmission frequency. For the simulations, the height of the winding $h_{cu} = 7.5$ mm is fixed at the diameter of a standard litz wire with a copper cross section of 20 mm^2 , which leads to a current density of approximately 5 A/mm^2 for an estimated transmitter coil rms current of 100 A.

In the next step, all parameter combinations for the number of ferrite cores $N_{fe} \in [3, 5, 7]$, outer coil dimensions $W_{coil} \in 300\text{--}700 \text{ mm}$ and $L_{coil} \in 300\text{--}700 \text{ mm}$, a width of the winding $w_{cu} \in 50\text{--}150 \text{ mm}$, and a position of the winding on the core $d_{cu} \in 50\text{--}150 \text{ mm}$ are evaluated in a parameter

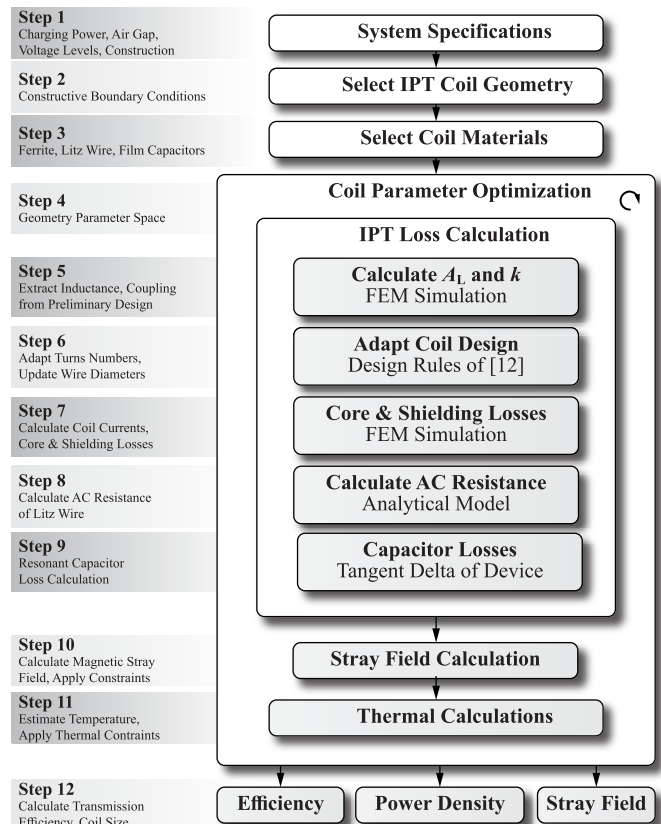


Fig. 5. Multi-objective coil optimization process based on a combination of FEM simulations and analytical calculations.

sweep using the FEM simulations and analytical calculations as described earlier (step 4).

In the first FEM simulation of each combination of geometry parameters (step 5), the A_L -value, defined as the ratio of the coil self-inductance and the turns number squared, and the magnetic coupling of the coil design are calculated. Since the magnetic coupling is unaffected by the modifications of the turns numbers as long as the winding dimensions remain the same, this value can subsequently be used for the design of the coil self-inductances without recalculation. Given the magnetic coupling, the required self-inductances are calculated according to the design rules of [14]

$$L_2 \approx \frac{R_{L,\text{eq}}}{\omega_0 k} \text{ and } L_1 \approx L_2 \left(\frac{U_{1,\text{dc}}}{U_{2,\text{dc}}} \right)^2 \quad (3)$$

where $R_{L,\text{eq}} = 8/\pi^2 \cdot U_{2,\text{dc}}^2/P_2$ represents the equivalent load resistance of the fundamental frequency model, P_2 represents the output power, and $U_{1,\text{dc}}$ and $U_{2,\text{dc}}$ stand for the transmitter and receiver-side dc-link voltage, respectively. All values are given in Table I. The necessary primary and secondary turns numbers N_1 and N_2 are derived from the required self-inductances using the A_L -value (step 6).

With the capacitance values selected for a full compensation of the self-inductances according to (2), the magnitude and the phase of the transmitter and receiver currents at $P_2 = 50 \text{ kW}$ output power and $U_{2,\text{dc}} = 800 \text{ V}$ receiver-side dc-link voltage can be determined using equivalent circuit equations. Then, the losses in the ferrite cores and the eddy current shielding,

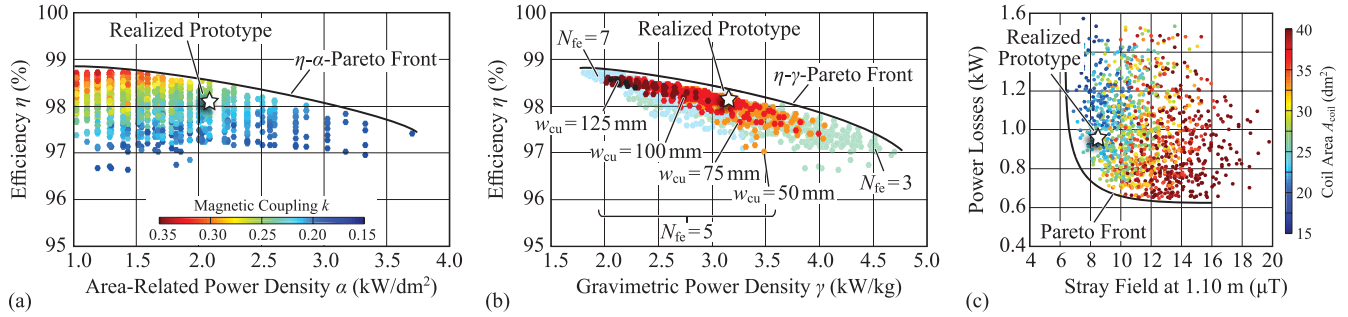


Fig. 6. Results of the multi-objective coil optimization. (a) η - α - and (b) η - γ -Pareto representation of the calculation results of the parameter sweep (power electronic converter not included). (c) Tradeoff between the total losses of the coil designs and the magnetic stray field at a fixed observation point.

as well as the magnetic stray field are determined for the actual operating point with a second FEM simulation (step 7).

For the calculation of the ac losses in the litz wire, the analytical winding loss model presented earlier is used (step 8). The litz wire diameter is chosen such that the width of the winding w_{cu} is the same for the simulated solid copper region and the actual winding with N_1 or N_2 closely spaced individual conductors. The number of strands follows from the calculated litz wire diameter, the preselected strand diameter, and a litz wire packing factor of 0.45 that is estimated based on manufacturer data.

Next, the compensation capacitors are dimensioned taking into account the voltage and current ratings of the selected capacitor series. High-power polypropylene film capacitors of type CSP 120-200 with custom capacitance values are considered [38]. The main reasons are their good thermal stability, the low impact of humidity on their capacitance value, and the excellent loss characteristics up to high frequencies. According to the manufacturer, the dissipation factor of these devices is in the range of $1 - 1.4 \times 10^{-3}$ up to 100 kHz, from which the dielectric losses can be estimated (step 9).

In the last part of the optimization, constraints on the stray field can be applied (step 10). The component temperatures are estimated with the thermal model (step 11) and compared with the maximum temperature ratings of the materials. A maximum surface temperature of $T_{max} \approx 120$ °C is considered for the litz wire winding as well as for the ferrite cores. Coil designs that violate these constraints are discarded from the results. For the remaining designs, the performance factors of interest are stored in a database (step 12).

C. Discussion of the Optimization Results

The calculated transmission efficiency η for the evaluated coil designs is shown as a function of the area-related power density α in Fig. 6(a) and as a function of the gravimetric power density γ in Fig. 6(b). Included are the losses in the litz wire windings, the ferrite core losses, the losses in the resonant capacitors, and the eddy current losses in the shielding. The area-related power density is defined as $\alpha = P_2/A_{coil}$, where $A_{coil} = L_{coil}W_{coil}$ represents the active area covered by the receiver coil on the EV. The gravimetric power density is given by $\gamma = P_2/m_{coil}$, where m_{coil} stands for the active mass of one IPT coil, including the ferrite cores, the eddy current shielding, the litz wire winding, and the weight of the capacitors.

For smaller coils with a higher area-related power density α , the magnetic coupling k is lower due to the smaller active coil area (see coloring in Fig. 6(a)). Thus, the transmission efficiency η is reduced. However, the smaller size of the transmission coils also leads to a lower active mass and therefore to a higher gravimetric power density γ . At the performance limit, the area-related power density α or the gravimetric power density γ can only be increased at the cost of a lower transmission efficiency η . This design tradeoff is described by the η - α - and the η - γ -Pareto fronts, which are drawn schematically in the figure.

The factors that determine the weight of the transmission coils are shown in Fig. 6(b). The most significant weight contribution is the weight of the ferrite core material. This confirms that the division of the core into parallel I -cores instead of a solid ferrite plate as proposed in [26] and [29] is a useful approach for weight reduction. Despite the reduced core cross section, the maximum core flux density is below 175 mT for all of the design points shown in the figures. The comparably low saturation flux density of the ferrite is therefore no limiting factor. Nevertheless, the hysteresis losses in the ferrite are higher for the designs with a lower number of cores N_{fe} due to the higher flux density, and consequently, the efficiency is lower. The weight of the litz wire winding is the second main component that determines the weight of the IPT coils. Coils with a lower winding width w_{cu} and consequently with a smaller copper cross section are lighter, but they have a lower efficiency as a result of the higher copper conduction losses. Fig. 6(c) shows the design tradeoff between the total losses of the calculated coil designs and the magnetic stray field. The observation point is located at a distance of 1.10 m on a laterally directed horizontal axis, which starts at the air gap center point. This is the closest point where humans could be exposed to the stray field if the coil is mounted to the EV chassis in the final arrangement. The metallic EV chassis itself is not considered for this worst case consideration, because it would have a damping effect on the magnetic stray field. The coloring in Fig. 6(c) represents the coil area A_{coil} of each design. A Pareto front exists at which for a further reduction of the magnetic stray field higher power losses must be accepted. At the boundary, the stray field can only be reduced if the magnetic field source, i.e., the IPT coil, is made smaller and the distance from the current carrying conductors to the observation point becomes longer. Hence, a

TABLE III
DESIGN PARAMETERS OF THE IPT COIL PROTOTYPE

Variable	Value
W_{coil} (mm)	380
L_{coil} (mm)	630
d_{cu} (mm)	125
w_{cu} (mm)	67.5
N_{fe}	5
N_1, N_2	9.5 ¹
C_1, C_2 (nF)	54.1
Litz wire	2500 x 0.1 mm
Ferrite cores	I-126/20, K2004
Resonant caps.	CSP 120-200
Shielding	OFC, 2 mm thick

¹TURNS NUMBER "9.5" MEANS THAT CONNECTIONS ARE AT OPPOSITE SIDES OF WINDING.

tradeoff is found between the coil size, the power losses, and the stray field.

For EV applications, a high area-related and gravimetric power density is mandatory for the vehicle-side system components. Comparing the results in Fig. 6(b), which include only the receiver coil and not the power electronics, to the gravimetric power density of 3.8 kW/kg of the 95% efficient conductive 6.1 kW EV charger in [39] highlights the low compactness as a main design challenge for IPT systems.

D. Coil Design Selected for Prototype

The design shown in Fig. 6 is selected for the realization of a hardware prototype. All the parameters of the selected IPT coil design are listed in Table III. When choosing the indicated design, all three Pareto fronts of Fig. 6 were closely inspected and an option with good performance in all aspects was manually selected in an iterative process. For this reason, the selected design point in the Pareto planes is located close to but not exactly on the Pareto fronts. For methodically identifying an optimal design, a mathematical cost function needs to be defined. However, the specification of the cost function would depend on several application specific factors that vary from case to case and is therefore not covered in this paper.

The individual contributions of the different components to the total losses of the selected design are shown in Fig. 7. Also the conduction losses in the SiC MOSFET devices (1.2 kV/25 mΩ, three discrete devices in parallel per switch) that are employed for the transmitter-side full-bridge inverter and the receiver-side synchronous rectifier at the receiver are listed for completeness.

As expected from the results that were obtained for the scaled system in [14], the loss contribution of the IPT coils and the resonant capacitors is approximately equal. Their respective shares on the total losses of the transmitter are 38% and 41%. The power semiconductors contribute the remaining 21% of the total losses. For the receiver, the loss distribution is similar. This is a result of the operation close to the efficiency optimum, which implies equal coil losses

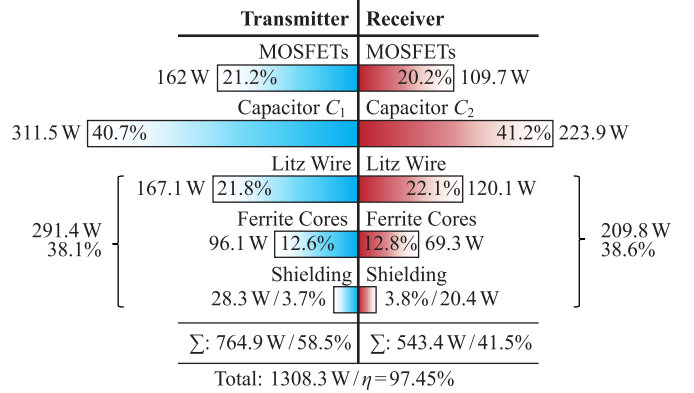


Fig. 7. Calculated power loss contributions of the resonant circuit components and the power semiconductors to the total losses of the realized IPT prototype.

on both sides of the air gap. Because of the synchronous rectification, also similar conduction losses result for the power semiconductors. The total losses amount to 1308.3 W, and hence, the calculated efficiency from full-bridge input to active rectifier output (from $U_{1,\text{dc}}$ to $U_{2,\text{dc}}$ in Fig. 1) is 97.45% at the maximum power transfer.

IV. PROTOTYPE REALIZATION

In this section, the practical aspects of the hardware realization of the optimized IPT coil design are discussed. First, the construction details of the coil and the capacitor module are presented. Afterward, the positioning tolerance of the IPT coils is analyzed, from which the requirements for the power electronic converter are determined. At the end of this section, an overview of the power electronic converter and the 50 kW experimental setup is given.

A. Realized Coil Prototype

Since induced eddy currents prohibit the use of metals for the structural elements of the IPT coils, the construction of the prototype relies on high-temperature plastic materials, such as polyoxymethylene (POM), polycarbonate, and Teflon, as shown in Fig. 8(a). For the base plate and the coil housing, POM parts produced by computerized numerical control (CNC) milling are employed. The ferrite cores are attached to the base plate with polycarbonate fixtures produced by additive manufacturing (3-D printing). Seamlessly integrated into the base plate is a core carrier produced from Teflon sheets by water jet cutting. The core carrier has a higher temperature rating than the POM base plate and can therefore be placed in direct contact with the ferrite cores without any risk of overheating. At the front and the back of the IPT coil, axial cooling fans are positioned via mounting points integrated into the base plate. To prevent air bleeding, the top of the coil is closed with a transparent polycarbonate cover. The winding is positioned on a CNC milled POM coil former. The coil former surface is realized with a grove structure for guiding the cooling air along the bottom side of the litz wire conductors. Milled guides on the coil former and 3-D printed polycarbonate fixture elements are used to hold the conductors in position. The coil former with the attached winding is then

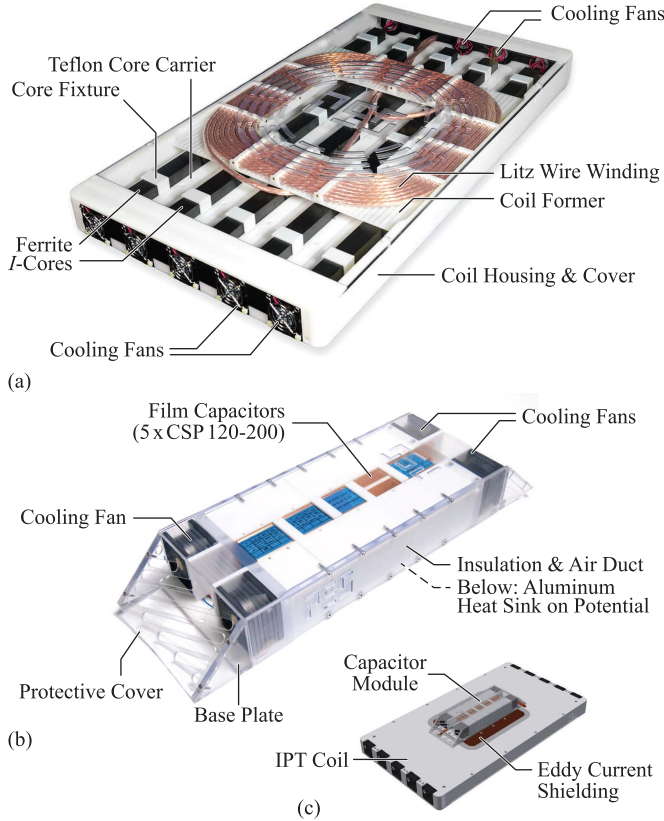


Fig. 8. (a) Photograph of the realized forced-air cooled 50 kW/85 kHz IPT coil prototype (transmitter and receiver coil are identical). (b) Photograph of the resonant capacitor module with forced-air cooling system. (c) Mounting position of the capacitor module at the backside of the IPT coil.

positioned on the cores and is directly attached to the coil housing.

The resonant capacitors are assembled as a compact module, which is mounted directly to the backside of each IPT coil, as shown in Fig. 8(c). A forced-air cooling system is necessary for dissipating the capacitor losses. Therefore, CNC milled aluminum heat sink elements are mounted to the device terminals. A 3-D printed polycarbonate cover serves as air duct and as electrical insulation.

As a result of the added 9.9 kg passive weight of the base plate, the coil housing, the active-cooling system, and the resonant capacitor module with its heat sink and eddy current shielding, the total weight of the coil is 24.6 kg. Given the additional space needed for the housing and the cooling system, the coil area is increased from initially 24.0 dm^2 for only the active components to 31.2 dm^2 by adding the passive parts. This finally results in an area-related power density 1.6 kW/dm^2 and a gravimetric power density of 2 kW/kg (or 907 W/lb) for the realized prototype.

B. Analysis of Coil Misalignment

In order to determine the necessary current carrying capability and the requirements for the cooling system of the IPT coils, the resonant capacitors, and the power electronics, the worst case rms coil currents are considered. These factors, together with the employed control scheme, ultimately limit the misalignment tolerance of the system. As soon as the

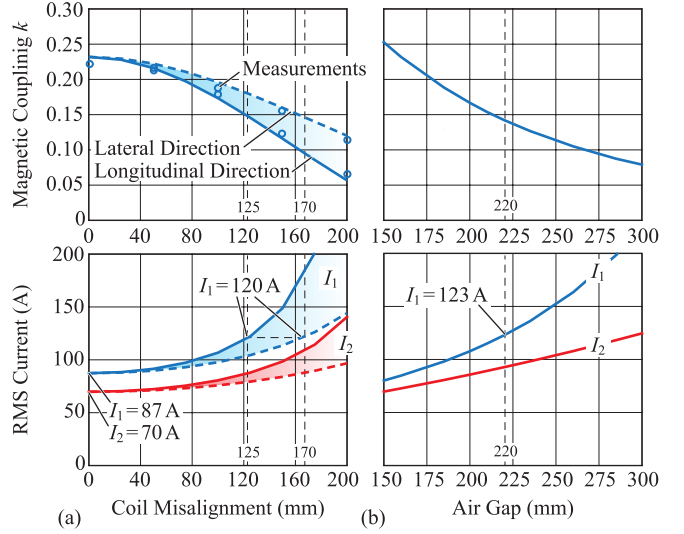


Fig. 9. FEM-calculated and measured magnetic coupling k , and required transmitter and receiver rms currents I_1 and I_2 for 50 kW power transfer as a function of (a) horizontal coil misalignment and (b) air gap between the IPT coils.

maximum currents or the maximum cooling capability is reached during operation, the only option is to limit the coil currents by decreasing the output power, which means charging the EV battery at a lower current and increased charging time.

Fig. 9 shows the FEM-calculated and measured magnetic coupling, as well as the respective rms coil currents for the transmission of 50 kW as a function of the horizontal coil misalignment and the air gap between the IPT coils. The currents are calculated using the highly accurate models presented in [40], which include the losses in the resonant system and also the influence of the nonlinear charging processes of the MOSFET capacitances during the ZVS switching transitions for the current calculation. The maximum efficiency control scheme of [14] and [41] is assumed.

As shown in Fig. 9(a), if the components are dimensioned for an rms current of 120 A, a positioning tolerance of $\pm 125 \text{ mm}$ is possible in the longitudinal direction. In this case, a coil misalignment of up to $\pm 170 \text{ mm}$ is tolerable in the lateral direction, and the operation at an air gap of up to approximately 220 mm is possible, as shown in Fig. 9(b).

The nominal currents are $I_1 = 87 \text{ A}$ and $I_2 = 70 \text{ A}$. Hence, the electronics are dimensioned for approximately 40% higher rms currents. For the worst case coil positioning, the power losses in IPT coils, the capacitors, and the power semiconductors are approximately doubled compared with an ideal coil positioning. Therefore, a significantly larger cooling system and higher current ratings are needed for the components, which limit the attainable power density of the contactless EV charger. This inherent necessity for overdimensioning of the components is another major disadvantage compared with a conventional conductive EV charger.

C. Power Electronics and Experimental Setup

Based on the calculated rms currents, the converter can be dimensioned. A fully detailed discussion of the power

electronics design can be found in a separate paper [21]. Herein, only a short summary of the selected converter topology and the control of the IPT system is given in order to facilitate the understanding of the measurements presented in Section V.

Typical IPT power converters employ a ZVS full-bridge inverter for the supply of a high-frequency ac voltage to the resonant circuit at the transmitter side. The power flow can be controlled either via the inverter switching frequency or the duty cycles of the inverter and the active rectifier stage. Recently, also the solutions with additional, external dc-dc conversion stages have been proposed [17], [18], [41], which is also the solution preferred in this paper. In this case, the two dc-link voltages $U_{1,\text{dc}}$ and $U_{2,\text{dc}}$ are used for the control of the power flow at a constant switching frequency and duty cycle. In this way, the resonant circuit is operated at its natural efficiency optimum with minimum switching losses in the full-bridge inverter and the active rectifier. In order to limit the necessary hardware effort, the identical IPT coils were designed in Section III, and the identical power converters are used for the receiver and the transmitter.

The selected converter topology is shown in Fig. 10(b). At the transmitter side, the full-bridge inverter stage is used to supply a 85 kHz rectangular voltage waveform with a constant 50% duty cycle to the resonant circuit, as shown in Fig. 10(c). At the receiver side, the same full-bridge serves as a synchronous rectifier. A measurement of the receiver coil current and a phase-locked loop in an Field Programmable Gate Array is used to generate the synchronous gate signals. Considering the high switching frequency of 85 kHz, SiC MOSFETs devices of type C2M0025120D with 1.2 kV blocking capability are used for the low ZVS losses. Three parallel connected devices with 25 mΩ ON-state resistance in TO-247 housings are used for each switch of the full bridge in order to achieve low conduction losses.

For regulating the dc-link voltages $U_{1,\text{dc}}$ and $U_{2,\text{dc}}$ as required for control of the power flow, a modular dc-dc stage comprising three parallel interleaved buck+boost type converters is used. The selected topology is shown in Fig. 10(b). In each module, two phases with 80 mΩ-SiC MOSFETs of type C2M0080120D, hard-switched at 50 kHz, are parallel interleaved. Coupled magnetic components are used for achieving a high compactness of the dc-dc converter modules.

For the experiments presented in Section V, the test setup with an energy feedback at the dc link shown in Fig. 10(a) is used. The energy feedback via the air-core inductor $L_{\text{fb}} = 3.4 \text{ mH}$ allows circulating the transferred power of up to 50 kW within the system, instead of dissipating the energy in a resistive load. While the transferred power is circulated, the total losses are covered by the external dc supply. Hence, the dc current I_{loss} and the dc supply voltage U_{batt} can be measured to determine the total power losses. The transferred power is found using a measurement of I_{fb} . In order to eliminate the dc losses in the feedback inductor from the total loss measurement results, the voltage drop across L_{fb} is measured in addition. The dc currents I_{loss} and I_{fb} are measured using the precision shunt resistors $R_1 = 10 \text{ mΩ}$ and $R_2 = 1 \text{ mΩ}$. The shunt voltages, the voltage drop on the

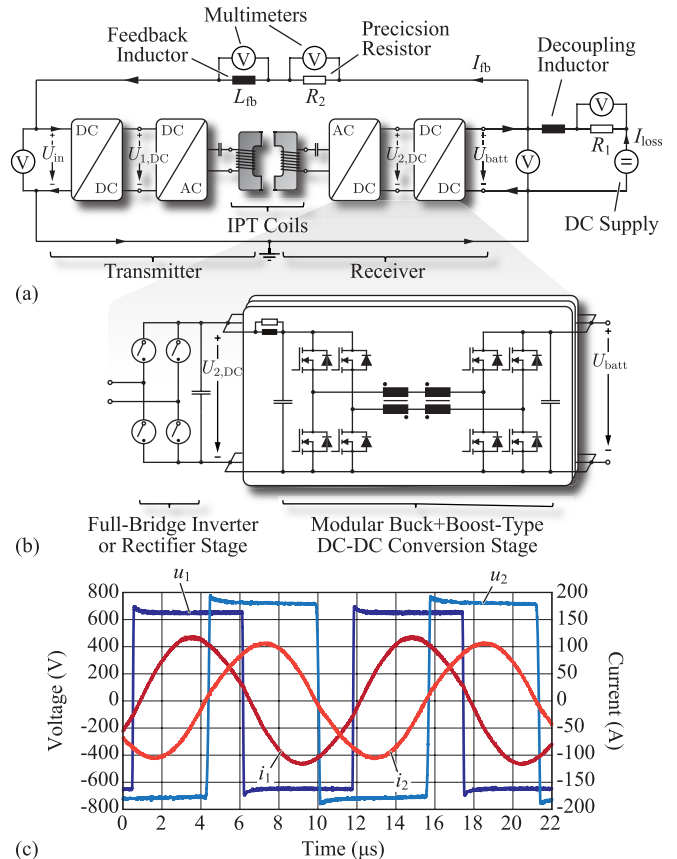


Fig. 10. (a) Experimental setup with energy feedback for direct power loss and efficiency measurements at up to 50 kW circulating power. (b) Topology of the two identical power converters at the transmitter and the receiver. (c) Waveforms of the transmitter-side full-bridge inverter output voltage u_1 , the transmitter coil current i_1 , the receiver coil current i_2 , and the receiver-side active rectifier input voltage u_2 , measured at 50 kW output power and $U_{\text{batt}} = 600 \text{ V}$ output voltage.

feedback inductor, and the dc supply voltage are measured with Agilent 34410A multimeters.

V. EXPERIMENTAL RESULTS

In this section, the comprehensive experimental results for the optimized IPT system are presented. Direct power loss measurements are performed on the experimental setup introduced earlier. The dc-dc efficiency of the IPT system is extracted and the component temperatures are documented. To conclude the experimental investigation, the magnetic stray field is measured with the magnetic field probe of [42].

A. DC-DC Efficiency Measurement

For the efficiency measurements, the transmitted power is controlled by adjusting the dc-link voltages $U_{1,\text{dc}}$ and $U_{2,\text{dc}}$ between 0 and 800 V according to the control scheme described in [41], using the dc-dc converter modules and the fixed supply voltage $U_{\text{batt}} = 600 \text{ V}$. Neglecting the losses in the system, the transmitted power then follows [14] as

$$P_2 \approx \frac{8}{\pi^2} \frac{U_{1,\text{dc}} U_{2,\text{dc}}}{\omega_0 M}. \quad (4)$$

During the measurement process, the active-cooling systems of the converter and of the IPT coils are constantly running.

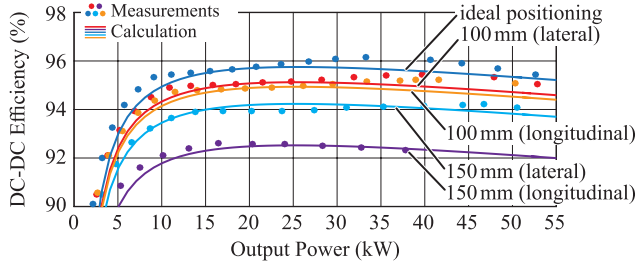


Fig. 11. Calculated and measured dc-dc efficiency for an air gap of 160 mm and variable horizontal coil misalignment at $U_{\text{batt}} = 600$ V. The positioning tolerance is higher in the lateral direction.

Thermal steady state is always ensured for all components, before the samples are taken. At each operating point, the dc voltages U_{in} and U_{batt} and the dc currents I_{loss} and I_{fb} are measured to determine the transmitted power and the losses.

The measured efficiency from the dc input U_{in} to the battery voltage U_{batt} with ideally aligned IPT coils at an air gap of 160 mm is shown in Fig. 11 together with the calculation results. The measurements include the complete power conversion chain, i.e., the ZVS full-bridge inverter, the synchronous rectifier, two dc-dc conversion stages, the resonant capacitors, and the IPT coils. The peak efficiency of 96.16% is measured at 33.2 kW. At 50 kW power transmission an efficiency of 95.8% is reached.

After the experiments with ideally positioned IPT coils, the measurements with horizontally misaligned coils are taken. The efficiency is decreased by approximately 0.7%-points for a lateral or longitudinal coil misalignment of 100 mm. A coil misalignment of 150 mm in the lateral direction leads to an efficiency reduction of close to 2%-points. An efficiency reduction of 3.8%-points to approximately 92% is observed at a longitudinal coil misalignment of 150 mm.

Due to the high frequency of the power transmission and the high voltage and current amplitudes, a measurement of the power losses of each individual component in the resonant circuit is not possible with acceptable accuracy, even with a power analyzer. Already small errors for the current and voltage phase shifts would lead to false results. A measurement of the ac resistance of the coil with an impedance analyzer is challenging as well. Based on the calculated ac resistance, a phase angle of 89.96° is expected for the coil impedance at 85 kHz. Thus, the angular difference of 0.04° with respect to a phase angle of 90° needs to be resolved with an accuracy of 0.004° for a measurement of the ac resistance with a 10% measurement error. This is beyond the capabilities of typical devices [43]. In addition, given the low value of the ac resistance to be measured, the impedance of the physically large probe fixture could adversely affect the accuracy of an impedance measurement. Therefore, the presented measurement of the total dc-dc efficiency based on a direct power loss measurement in the setup with circulating power is considered the best option for the model verification.

B. Component Temperature Measurements

In order to validate the thermal management of the IPT coil with forced-air cooling, temperature measurements

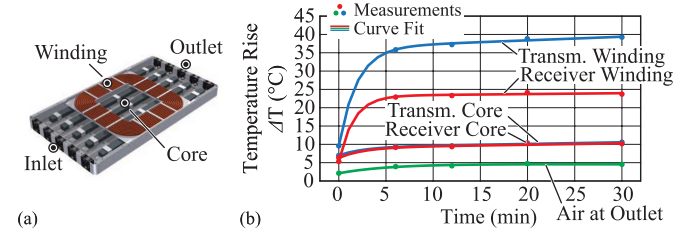


Fig. 12. (a) Positions of the thermocouples for the measurement of the component temperatures. (b) Measured transmitter and receiver winding temperatures, core temperatures, and air temperature at the outlet of the cooling system during continuous operation with 50 kW power transmission.

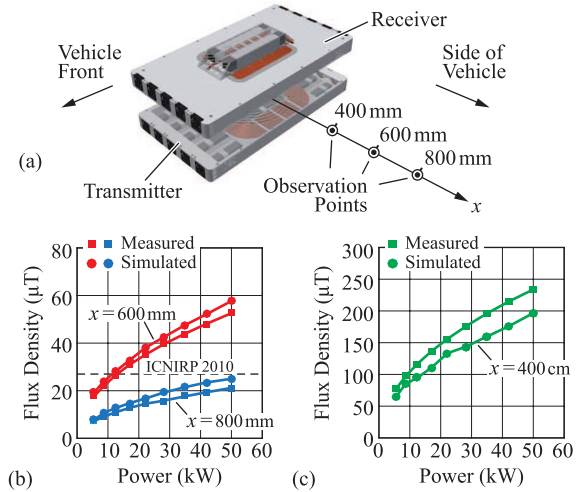


Fig. 13. (a) Measurement setup for the evaluation of the magnetic stray field. Measured and FEM-calculated rms magnetic flux density at (b) 800, 600, and (c) 400 mm lateral distance from the air gap center point.

are conducted, while the IPT system is continuously operating with 50 kW power transmission and ideally positioned IPT coils. The core and winding temperatures are measured with thermocouples that are glued to the litz wire and to the core. In addition, the air temperatures are measured with two thermocouples at the inlet and at the outlet of the cooling system. The sensor positions are shown in Fig. 12(a). The air temperature measured at the inlet, approximately $T_{\text{amb}} \approx 24$ °C during the measurements, is used as the reference temperature for the calculation of the temperature rise $\Delta T = T - T_{\text{amb}}$. The measured component temperatures are shown in Fig. 12(b). The temperatures of the litz wire and the cores stay well below the maximum ratings of the materials.

C. Measurement of the Magnetic Stray Field

For the verification of the magnetic stray field calculation, the magnetic field probe designed in [22] and [42] is used. The field probe is consecutively positioned at three observation points, as shown in Fig. 13(a). For every point, the power transfer of the IPT system is increased stepwise. The obtained measurement results are compared with the FEM calculations for the same observation points in Fig. 13(b).

The calculated magnetic stray fields exhibit an error of approximately 15% with respect to the measured values. Several aspects could explain the observed deviation. Firstly, the measurements for the 50 kW system are conducted in a

Faraday cage for safety reasons. This means that the experimental setup is arranged in a relatively narrow area surrounded by a grounded metal fence. Additional metals are present in the power supply, the cabling, and the measurement equipment. Eddy currents are induced in all of these metal parts, which distorts the magnetic field distribution. These effects are not modeled in the FEM simulation. Secondly, the FEM model contains model simplifications, which could adversely affect the calculation accuracy. For instance, the resonant capacitor module mounted to the back of the IPT coil is not included in the FEM model in order to accelerate the convergence of the solver.

The presented measurements show that the designed IPT system fulfills the ICNIRP 2010 guidelines [16] for the magnetic field exposure of the general public at a distance of 800 mm from the coil center up to the full power of 50 kW.

VI. CONCLUSION

In this paper, the multi-objective optimization of an IPT system for public transport EV charging was presented. The main aim of the underlying industry research project is to answer the question of how a fully optimized contactless EV charger compares with a conventional conductive charger, and what performance is possible if all system components are optimized in a holistic design approach. Therefore, a 50 kW hardware demonstrator was practically realized and experimentally tested as a benchmark. The measured dc–dc efficiency is 95.8% at 50 kW for the prototype coil with a power density 1.6 kW/dm² and 2 kW/kg (or 907 W/lb), including all power electronics stages.

The presented multi-objective IPT optimization process provides a systematic approach for taking the technological limits and Pareto tradeoffs into account during the design phase. The method allows analyzing multiple performance aspects simultaneously while considering all relevant boundary conditions, such as the limitation of the high-frequency electromagnetic stray fields or the thermal feasibility. In this way, it is possible to find a balanced IPT system design, which satisfies all performance requirements simultaneously.

The analysis of the encountered performance tradeoffs highlights the limitations of IPT for EV charging. For a practical realization in the automotive industry, highly compact IPT coils are required due to the limited construction volume on the EV, for reducing the magnetic stray field at high power levels, and to lower the material cost. This is a major design challenge, because a reduction of the IPT coil size is always tied to a Pareto tradeoff with the transmission efficiency that is largely governed by the physics of the contactless transformer and the geometric arrangement in the target application.

ACKNOWLEDGMENT

The authors would like to thank ABB Switzerland Ltd. for their support regarding many aspects of this research project.

REFERENCES

- [1] Electric Vehicles Initiative of the International Energy Agency. (2013). *Global EV Outlook: Understanding the Electric Vehicle Landscape to 2020*, accessed on Sep. 11, 2015. [Online]. Available: <http://www.iea.org/evi>
- [2] Electric Vehicles Initiative of the International Energy Agency. (2015). *Global EV Outlook 2015*, accessed on Sep. 11, 2015. [Online]. Available: <http://www.iea.org/evi>
- [3] Chinabuses. (2012). *Shenzhen, China Launches the World's Largest Electric Vehicle Fleet*, accessed on Feb. 10, 2016. [Online]. Available: <http://www.chinabuses.org>
- [4] PR Newswire. (2015). *BYD Motors Wins America's Largest Electric Bus Order*, accessed on Feb. 10, 2016. [Online]. Available: <http://www.prnewswire.com>
- [5] B. Warner, O. Augé, and A. Moglestue, “Taking charge—Flash charging is just the ticket for clean transportation,” *ABB Rev.*, no. 4, pp. 64–69, 2013, accessed on Feb. 24, 2016. [Online]. Available: <http://www.abb.com>
- [6] Siemens AG. (2015). *Charging Your Future—with the Siemens eBus Charging Infrastructure*, accessed on Sep. 16, 2015. [Online]. Available: <http://www.siemens.com/mobility>
- [7] Conductix Wampfler/Delachaux SA. (2012). *10 Years of Electric Buses With IPT Charge*, accessed on Sep. 16, 2015. [Online]. Available: <http://www.conductix.com>
- [8] Bombardier Transportation. (2013). *Primove—Introducing True Electric Mobility for a Sustainable Future*, accessed on Sep. 16, 2015. [Online]. Available: <http://primove.bombardier.com>
- [9] Wave IPT. (2015). *Wirelessly Charging Electric Vehicles*, accessed on Sep. 16, 2015. [Online]. Available: <http://www.waveipt.com>
- [10] S. Y. Choi, B. W. Gu, S. Y. Jeong, and C. T. Rim, “Advances in wireless power transfer systems for roadway-powered electric vehicles,” *IEEE J. Emerg. Sel. Topics Power Electron.*, vol. 3, no. 1, pp. 18–36, Mar. 2015.
- [11] D. Magnor, J. B. Gerschler, M. Ecker, P. Merk, and D. U. Sauer, “Concept of a battery aging model for lithium-ion batteries considering the lifetime dependency on the operation strategy,” in *Proc. 24th Eur. Photovoltaic Solar Energy Conf.*, Hamburg, Germany, Sep. 2009, pp. 3128–3134.
- [12] E. H. Lechner and S. E. Schladoer, “The roadway powered electric vehicle—An all-electric hybrid system,” in *Proc. 8th Int. Electr. Vehicle Symp.*, Washington, DC, USA, Oct. 1986, pp. 248–257.
- [13] G. A. Covic and J. T. Boys, “Inductive power transfer,” *Proc. IEEE*, vol. 101, no. 6, pp. 1276–1289, Jun. 2013.
- [14] R. Bosshard, J. W. Kolar, J. Mühlthaler, I. Stevanović, B. Wunsch, and F. Canales, “Modeling and η - α -Pareto optimization of inductive power transfer coils for electric vehicles,” *IEEE J. Emerg. Sel. Topics Power Electron.*, vol. 3, no. 1, pp. 50–64, Mar. 2015.
- [15] E. Waffenschmidt and T. Staring, “Limitation of inductive power transfer for consumer applications,” in *Proc. 13th Eur. Conf. Power Electron. Appl. (EPE-ECCE Europe)*, Barcelona, Spain, Sep. 2009, pp. 1–10.
- [16] International Commission on Non-Ionizing Radiation Protection, “Guidelines for limiting exposure to time-varying electric and magnetic fields (1 Hz to 100 kHz),” *Health Phys.*, vol. 99, no. 6, pp. 818–836, 2010.
- [17] B. Goeldi, S. Reichert, and J. Tritschler, “Design and dimensioning of a highly efficient 22 kW bidirectional inductive charger for E-mobility,” in *Proc. Int. Exhibit. Conf. Power Electron. (PCIM Europe)*, Nuremberg, Germany, 2013, pp. 1496–1503.
- [18] J. Tritschler, S. Reichert, and B. Goeldi, “A practical investigation of a high power, bidirectional charging system for electric vehicles,” in *Proc. 16th Eur. Conf. Power Electron. Appl. (EPE-ECCE Europe)*, Lappeenranta, Finland, 2014, pp. 1–7.
- [19] P. Schumann, O. Blum, J. Eckhardt, and A. Henkel, “High efficient, compact vehicle power electronics for 22 kW inductive charging,” in *Proc. 4th Int. Electr. Drives Prod. Conf. (EDPC)*, Nuremberg, Germany, Sep./Oct. 2014, pp. 1–5.
- [20] A. Pevere, R. Petrella, C. C. Mi, and S. Zhou, “Design of a high efficiency 22 kW wireless power transfer system for EVs fast contactless charging stations,” in *Proc. Int. Electr. Vehicle Conf. (IEVC)*, Florence, Italy, Dec. 2014, pp. 1–7.
- [21] R. Bosshard and J. W. Kolar, “All-SiC 9.5 kW/dm³ on-board power electronics for 50 kW/85 kHz automotive IPT system,” *IEEE J. Emerg. Sel. Topics Power Electron.*, to be published.
- [22] R. Bosshard, “Multi-objective optimization of inductive power transfer systems for EV charging,” Ph.D. dissertation, Dept. Inf. Technol. Elect. Eng., ETH Zurich, Zürich, Switzerland, 2015.
- [23] R. Bosshard and J. W. Kolar, “Inductive power transfer for electric vehicle charging—Technical challenges and trade-offs,” *IEEE Power Electron. Mag.*, vol. 3, no. 3, Sep. 2016.
- [24] L. K. L. Cheng, J. W. Hay, and P. G. W. Beart, “Contact-less power transfer,” U.S. Patent 6 906 495 B2, Jun. 14, 2005.

- [25] J. T. Boys, G. A. Covic, and M. B. Budhia, "Inductive power transfer apparatus," WO Patent 2012018268 A1, Feb. 9, 2012.
- [26] C.-Y. D. Huang, "Design of IPT EV battery charging systems for variable coupling applications," Ph.D. dissertation, Dept. Elect. Comput. Eng., Univ. Auckland, Auckland, New Zealand, 2011.
- [27] M. Budhia, J. T. Boys, G. A. Covic, and C.-Y. Huang, "Development of a single-sided flux magnetic coupler for electric vehicle IPT charging systems," *IEEE Trans. Ind. Electron.*, vol. 60, no. 1, pp. 318–328, Jan. 2013.
- [28] R. Bosshard, U. Iruretagoyena, and J. W. Kolar, "Comprehensive evaluation of rectangular and double-D coil geometry for 50 kW, 85 kHz IPT system," *IEEE J. Emerg. Sel. Topics Power Electron.*, to be published.
- [29] N. P. Suh, S. H. Chang, D. Cho, G. H. Cho, C. T. Rim, and J. G. Cho, "Ultra slim power supply device and power acquisition device for electric vehicle," U.S. Patent 8 833 533 B2, Sep. 16, 2014.
- [30] J. Mühllethaler, "Modeling and multi-objective optimization of inductive power components," Ph.D. dissertation, Dept. Inf. Technol. Elect. Eng., ETH Zurich, Zürich, Switzerland, 2012.
- [31] A. Van den Bossche and V. C. Valchev, *Inductors and Transformers for Power Electronics*. New York, NY, USA: Taylor & Francis, 2005.
- [32] C. Gammeter, F. Krismer, and J. W. Kolar, "Weight optimization of a cooling system composed of fan and extruded-fin heat sink," *IEEE Trans. Ind. Appl.*, vol. 51, no. 1, pp. 509–520, Jan./Feb. 2015.
- [33] J. Biela and J. W. Kolar, "Cooling concepts for high power density magnetic devices," in *Proc. Power Convers. Conf. (PCC)*, Nagoya, Japan, Apr. 2007, pp. 1–8.
- [34] K. van Schuylenbergh and R. Puers, *Inductive Powering: Basic Theory and Application to Biomedical Systems*, 1st ed. Dordrecht, The Netherlands: Springer, 2009.
- [35] *Wireless Charging of Electric and Plug-in Hybrid Vehicles*, Society of Automotive Engineers, SAE Standard. J2954 (unpublished), accessed on Sep. 16, 2015. [Online]. Available: <http://standards.sae.org/wip/j2954/>
- [36] Society of Automotive Engineers (SAE). (2013). *Press Release ID 2296*, accessed on Sep. 16, 2015. [Online]. Available: <http://www.sae.org>
- [37] Kaschke Components GmbH. (2015). *I-Kern I 126/20 Data Sheet*, accessed on Jun. 17, 2016. [Online]. Available: <http://www.kaschke.de>
- [38] Celem Power Capacitors Ltd. (2015). *CSP 120/200 Data Sheet*, accessed on Jun. 17, 2016. [Online]. Available: <http://www.celem.com>
- [39] B. Whitaker *et al.*, "A high-density, high-efficiency, isolated on-board vehicle battery charger utilizing silicon carbide power devices," *IEEE Trans. Power Electron.*, vol. 29, no. 5, pp. 2606–2617, May 2014.
- [40] O. Knecht, R. Bosshard, and J. W. Kolar, "High-efficiency transcutaneous energy transfer for implantable mechanical heart support systems," *IEEE Trans. Power Electron.*, vol. 30, no. 11, pp. 6221–6236, Nov. 2015.
- [41] R. Bosshard, J. W. Kolar, and B. Wunsch, "Control method for inductive power transfer with high partial-load efficiency and resonance tracking," in *Proc. Int. Power Electron. Conf. (IPEC-ECCE ASIA)*, Hiroshima, Japan, May 2014, pp. 2167–2174.
- [42] R. Bosshard, J. W. Kolar, and B. Wunsch, "Accurate finite-element modeling and experimental verification of inductive power transfer coil design," in *Proc. 29th Appl. Power Electron. Conf. Expo. (APEC)*, Fort Worth, TX, USA, 2014, pp. 1648–1653.
- [43] S. Prabhakaran and C. R. Sullivan, "Impedance-analyzer measurements of high-frequency power passives: Techniques for high power and low impedance," in *Proc. Conf. Rec. 37th Annu. Meeting IEEE Ind. Appl. Soc. (IAS)*, vol. 2. Pittsburgh, PA, USA, Oct. 2002, pp. 1360–1367.



Roman Bosshard (S'10) received the M.Sc. and Ph.D. degrees from the Swiss Federal Institute of Technology (ETH) Zürich, Zürich, Switzerland, in 2011 and 2015, respectively.

He focused on power electronics, ultrahigh-speed electrical drives, and control of mechatronic systems, during his studies. In 2011, he joined the Power Electronic Systems Laboratory, ETH Zürich, where he was a Ph.D. student and a Post-Doctoral Researcher. In 2016, he joined ABB Switzerland Ltd., Turgi, Switzerland, as a Power Electronics Development Engineer. His current research interests include inductive power transfer systems, high-power converter systems, SiC wide bandgap power devices, and electric drive systems.



Johann W. Kolar (M'89–SM'04–F'10) is currently a Full Professor and the Head of the Power Electronic Systems Laboratory with the Swiss Federal Institute of Technology (ETH) Zürich, Zürich, Switzerland. His current research interests include ultracompact and ultraefficient SiC and GaN converter systems, wireless power transfer, solid-state transformers, power supplies on chip, and ultrahigh speed and bearingless motors. He has authored over 650 scientific papers in international journals and conference proceedings and holds more than 120 patents.

Johann Kolar received 21 IEEE Transactions and Conference Prize Paper Awards, and the ETH Zurich Golden Owl Award for excellence in teaching.